

A SIMPLE APPROACH TO COMPUTATIONAL AEROELASTICITY OF NASA ROTOR 67

R. Wiranegara^{*,†}, A. Turan^{*,‡}

^{*}School of Mechanical, Aerospace and Civil Engineering, The University of Manchester,
The George Begg Building, Manchester, M1 3BB, UK

[†]raditya.wiranegara@manchester.ac.uk; [‡]a.turan@manchester.ac.uk

Keywords: *CFD, NASA Rotor 67, Aeroelasticity, Near Stall*

Abstract

NASA rotor 67 has been the most commonly research apparatus for the study of aeroelasticity. It is the first single stage of a transonic axial fan. The present work is conducted using a commercial three dimensional finite volume CFD package, FLUENT. The simulation runs in a time-dependent manner such that the unsteady flow phenomenon could be captured which accounts for the pressure and viscous forces variations. The coupled bending-torsion equations are essentially 4th order parabolic and 2nd order hyperbolic partial differential equations. However, the type of the coupled equations used within the current work is similar to the one used on the rotorcraft blades structural coupling. The equations included a number of forces involved in a rotating blade, namely the centrifugal dan Coriolis forces. These equations are discretized with Finite Difference Method (FDM) by which was the simplest discretization method. A UDF is utilized with two roles, namely the spanwise forces plotter.

1 Introduction

The presence of unsteady aerodynamic loadings on a blade of jet engine due to shock waves and flow separation subjects the blade to either bend and/or twist modes of deformation. Moreover, there are demands for a newly-designed jet engine to meet the nowadays requirements, namely high trust to weight ratio and fuel efficiency [1]. The demand can only be fulfilled by reducing the blade thickness and

weight, thus lowering its stiffness. Stiffness plays an important part in the blade damping ability. Hence, the reduction of the blade stiffness conveys a physical consequence of a more susceptible blade to flow induced vibration. Following the inevitable consequence, it also raises a concern in the safety of the jet engine, particularly during its operation. A thin and light blade may lead to structural failure should the vibration exceed its material fatigue resistance to cyclic load.

As Doi [2] has pointed out, the induced vibration can either be stable, as seen in the case of forced vibrations due to inlet distortions or blade row interactions, or unstable, as seen in the case of self-excited vibrations or flutter. The latter receives a great deal of recognition as it is likely to occur.

Both the compressor and turbine blades of a jet engine are equally susceptible to flutter. However, the former is more likely to be exposed to flow disturbances such as inlet distortion due to gust, cross-winds and foreign object damage, the compressor stage flutter, or fan stage in a case of turbofan [3]. Hence, it receives a more critical attention.

Depending on the engine operating condition, the compressor is subjected to different types of flutter; see Fig. 1. There are at most four types of flutter, namely subsonic/transonic stall flutter, choke flutter, supersonic flutter, and supersonic stall flutter [4]. Subsonic/transonic stall flutter is encountered at ground conditions and during the flight at low altitude. The positive incidence causes the flow to separate on the pressure

surface of the blade. Due to the unsteadiness of the flow, the blade begins to vibrate as seen in the vortex shedding of a cylinder. The vibration shape mode is usually first torsion mode. Choke flutter appears in a region below the operating line. The exact cause of this type of flutter is still not well understood. Supersonic unstalled flutter occurs in either torsion or bending mode. The vibration mode is resulted from the involvement of the detaching bow shock wave which impinges the suction surface of the adjacent blade. The increasing pressure ratio causes the flow separation to grow in size. Supersonic stalled flutter is similar to subsonic stalled flutter as it is observed during positive incidence. Bending is the mode of the blade vibration for this type of flutter.

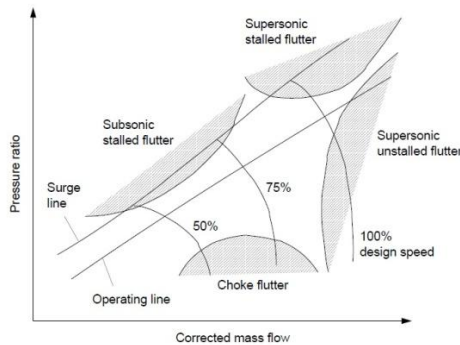


Fig. 1 Flutter projections in compressor map [4]

It has been said that stalled flutter is the main cause of compressor blade failure. Its occurrence is basically caused by the stalling of the flow about the blade. Unlike the classic flutter, as Boyce [5] explained, which is a coupled bending-torsion vibration developed if the free stream velocity surrounding the blade reaches critical flutter velocity.

Efforts have been carried out by many researchers to achieve flutter-free compressor. Identification of the boundaries of the flutter regime is one that can be done prior to preventing its occurrence. Khalak [6] in his paper provided four parameters related to flutter operability assessment, namely reduced damping, classical reduced frequency, characteristics inlet flow angle and characteristics inlet Mach number. A computational work by Martensson et al. [7] was focusing on flutter free compressor regimes and measuring the aerodynamic damping for a wide range of operating conditions. It was also

said here that negative aerodynamic damping is considered as the flutter limit, for a practical reason.

The paper proceeds by presenting the CFD simulation of NASA Rotor 67 and its validation against the experimental results by Strazisar et al [8]. Included here are the downstream, blade-to-blade profiles and aerodynamic forces on each spanwise sections obtained by employing a UDF. The discussion is followed by elaborating the coupled bending-torsion equations. The equations are in 1D, similar to one used in the structural analysis of rotorcraft blade.

2 NASA Rotor 67

2.1 About the Rotor

The rotor is a low aspect ratio rotor and part of the first stage of two stage transonic axial fan. The design specifications of the rotor are summarized in Table 1.

Some notable experimental works regarding the rotor flow field measurement of transonic viscous flow within the rotor was produced by Pierzga & Wood [9] and Strazisar et al.. The work included geometry details of the rotor blade.

Table 1 Design Specifications of NASA Rotor 67

Specifications	Values
Number of blades	22
Rotation speed	16043 RPM
Tip speed	429 m/s
Inlet tip relative mach number	1.38
Design mass flow rate	33.25 kg/s
Design pressure ratio	1.63
Design tip radius at leading edge	25.7 cm
Design tip radius at trailing edge	24.25
Hub to tip ratio at leading edge	0.375
Hub to tip ratio at trailing edge	0.478

2.2 Numerical tools

In the current work, the computational domain is meshed with structured H-type grid to ease out the meshing process. This type of grid was previously used by Yamada et al. [10], Khaleghi et al. [11] and Du et al. [12]. The domain contains a single blade passage of the

rotor. The grid has 68 nodes spanwise, 176 nodes streamwise (116 nodes on the blade) and 64 nodes on circumferential direction. Fig. 2 shows the grid.

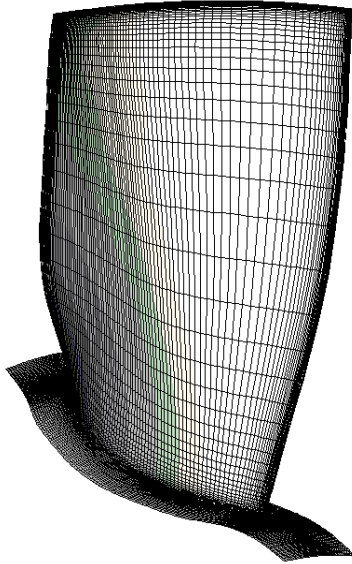


Fig. 2 The rotor computational domain and three dimensional grid

The boundary conditions are set according to the general boundary conditions for turbomachinery. This includes the inlet boundary condition, the exit boundary condition, the periodic boundary condition to handle the periodicity of turbomachinery flows and the solid wall boundary condition defined at the hub, the shroud and the blade.

At the inlet, the total pressure, the flow angle and the total temperature are set to be atmospheric pressure, perpendicular to the boundary and 288.15 K, respectively.

At the outlet, the pressure is the static pressure defined at the hub, namely 104729 Pa. The local static pressure is found by the use of radial equilibrium pressure distribution.

As for the turbulence models, the current work uses Spalart Allmaras (SA) and $k - \omega$ SST (Shear Stress Transport). The current work also does not account the gap between the clearance between the blade's tip and the shroud of the rotor housing.

2.3 Validations

The Mach number contours at three different spanwise positions, namely 10%, 30%

and 70% from the blade's tip, produced from the current work are showing quite comparable results with the experimental.

At 10%, the inlet relative Mach number is around 1.35. The current simulation result shows to be in between 1.3-1.4, see Fig. 3. From the experiment, it is seen that the highest resulting Mach number is 1.45 whilst in the current simulation is on 1.4. The shocks are reasonably depicted by the current simulation. The normal shock observed slightly off the leading edge of the blade can also be seen from the current simulation. Separation due to the interaction between the shock and boundary occurs at the mid-chord of the blade.

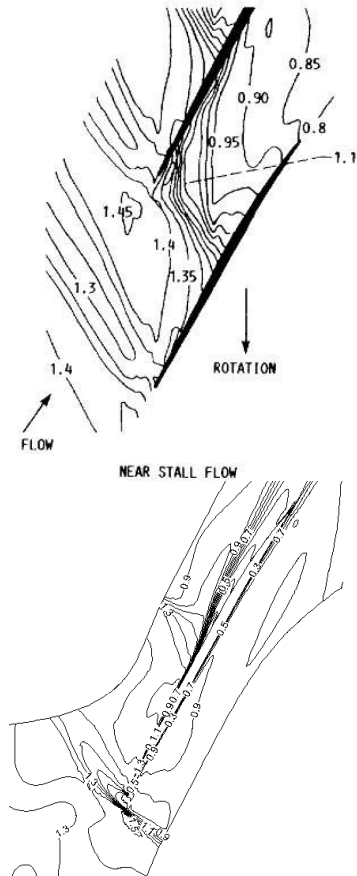


Fig. 3 10% span from the shroud Mach number contour (top: experiment; bottom: current simulation)

High Mach number is also observed at the 30% span of the blade; see Fig. 4. The flow structure is almost similar to the previous Mach number contour, i.e. the 10% span Mach number contour. The inlet relative Mach number of the experiment is between 1 to 1.35. From the simulation, it shows to be within 1 to 1.3.

At 70% span of the shroud, it is expected to show supersonic balloon at the blade leading edge. It is a balloon-like region that encapsulates the supersonic flows; see in Fig. 5. The simulation captures the balloon quite well.

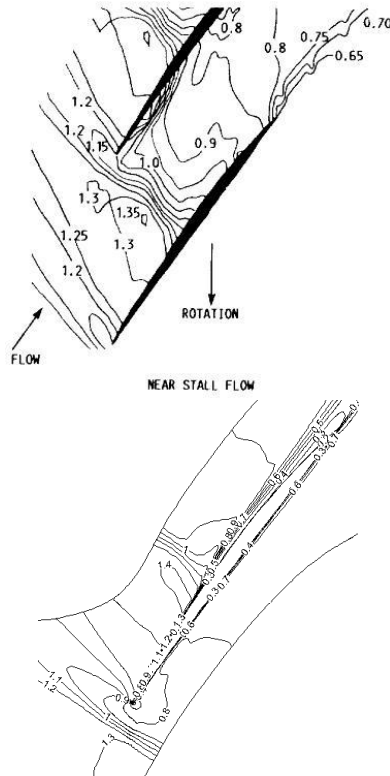


Fig. 4 30% span from the shroud Mach number contour

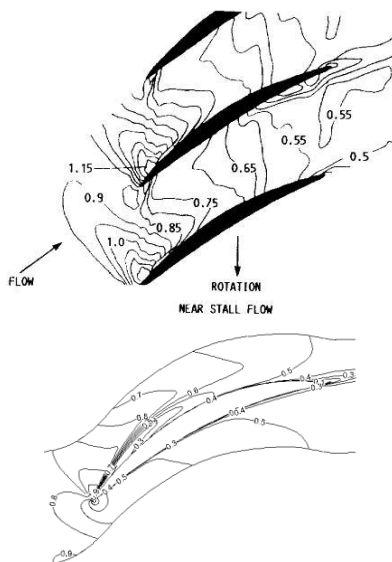


Fig. 5 70% span from the shroud Mach number contour

Fig. 6 to 9 show the downstream profiles for certain flow parameters, namely static pressure ratio, total pressure ratio, total

temperature ratio and flow angle, for both turbulence models.

The static pressure ratio profiles obtained from the current simulation, as presented in Fig. 6, fits quite reasonably well with the experiment.

Fig. 7 shows the total pressure ratio profiles. Discrepancy is seen around the mid-span of the blade. While near the tip and the hub, the current simulation predicted close enough as compared with the experiment.

Similarly, the total pressure ratio profiles near the hub fits perfectly with the experiment. Wide discrepancy with the experiment and the previous simulation appears at about 0.3 from the hub.

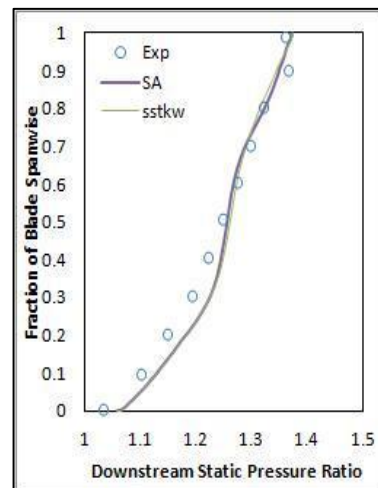


Fig. 6 Downstream Static Pressure Ratio Profiles

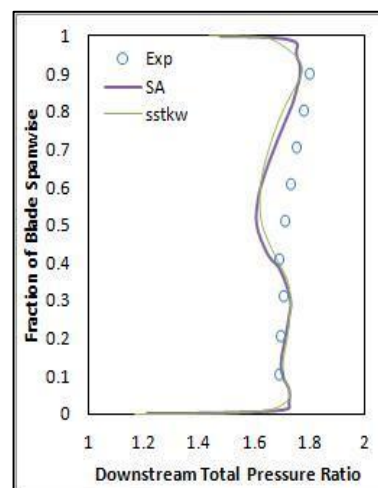


Fig. 7 Downstream Total Pressure Ratio Profiles

Discrepancies in the downstream flow parameters along the blade spanwise are also evident from Fig. 8 and 9, namely the total temperature and flow angle profiles.

Nevertheless, the trends show within these figures are comparable with the experiment.

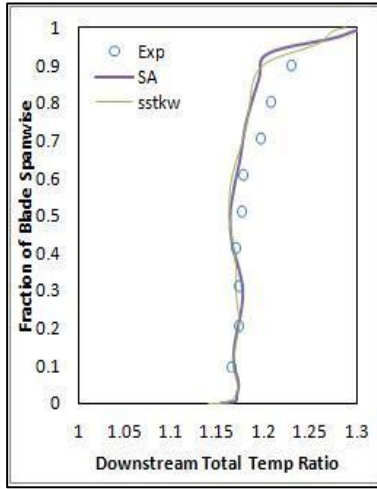


Fig. 8 Downstream Total Temperature Ratio Profiles

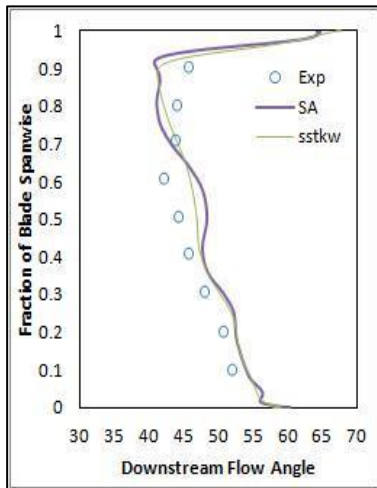


Fig. 9 Downstream Flow Angle Profiles

Normal shocks are well-observed, indicated by sudden Mach number drop, from the left graphs in and. Generally, the normal shock strength is measured based on the pressure ratio across the normal shock which can also be correlated with the Mach numbers from both sides. The correlation is written as follow.

$$\frac{p_2}{p_1} = \frac{(1 + \gamma Ma_1^2)}{(1 + \gamma Ma_2^2)} \quad (1)$$

$\frac{p_2}{p_1}$ is the pressure ratio across the shock, Ma_1 and Ma_2 are respectively the Mach number before and after the shock and γ is the ratio of specific heats (for air, approximately 1.4).

Fig. 10 is showing the profiles at two blade chordwise positions on the 10% blade spanwise. At 20% blade chordwise, there is wide

difference between the Mach numbers across the shock shown by both of the simulators. Using Equation (1), the pressure ratio across the normal shock of the current and previous simulations is found to be between 1.9-1.92 while the experiment is about 1.33. The discrepancy in the shock strength is, as Chima [13], Reis [14], Tang [15] and Adamczyk et al. [16], have pointed out, due to the absence of tip clearance. The tip clearance accounts for the formation of tip vortex resulted from the interaction of the flow between the pressure and suction sides of the blade hence affecting the performance [16]. At 123% blade chordwise, the profiles are qualitatively matched with the experiment and the previous simulation. Nevertheless, the magnitude differences can still be distinguished by which the tip clearance may have the effect on.

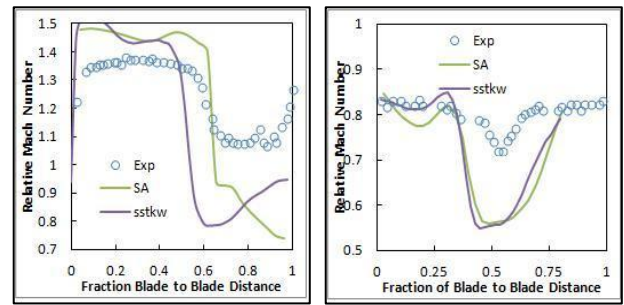


Fig. 10 10% spanwise at 20% & 123% chordwise position

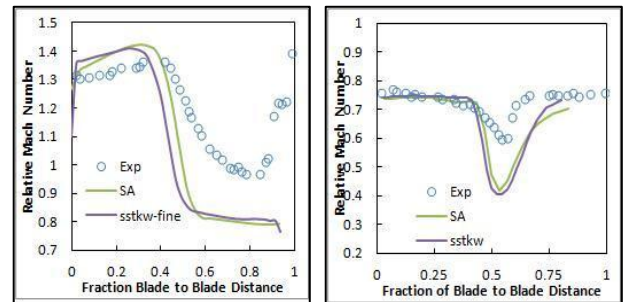


Fig. 11 30% spanwise at 20% & 118% chordwise position

The explanation also applied to the 118% and 110% blade chordwise positions at 30% and 70% blade spanwise; see the right-hand graphs in Fig. 11 and 12. Similarly, the left-hand graph in Fig. 10 also shows discrepancy of the shock strength in lower Mach number. Qualitatively, the profiles are indeed quite reasonable for both blade chordwise positions. No shock is observed from the left-hand graph in Fig. 11. As seen in

Fig. 5, the supersonic flow is contained in bubble-like region sitting at the blade leading edge. Hence, no sudden drop is found from the left-hand graph in Fig. 12. Instead, the Mach number gradually drops across the blade-to-blade distance.

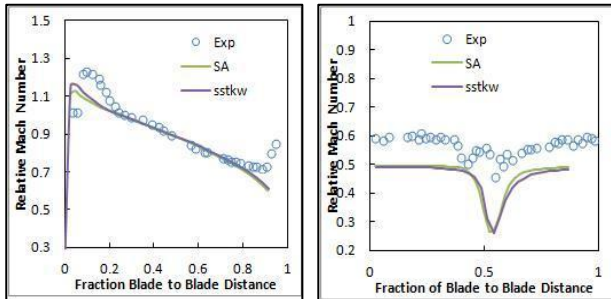
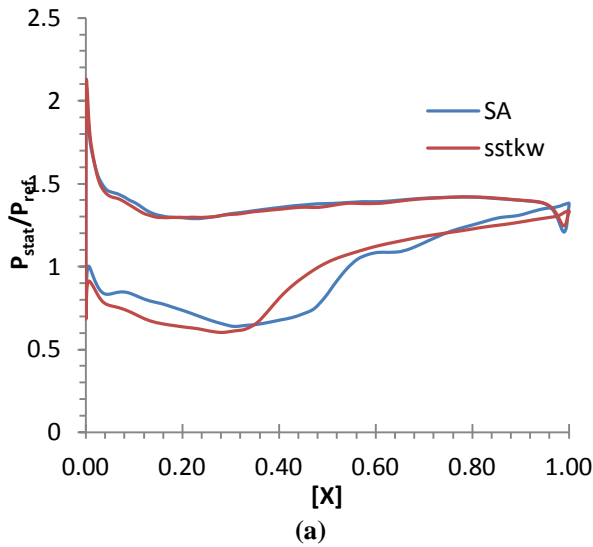
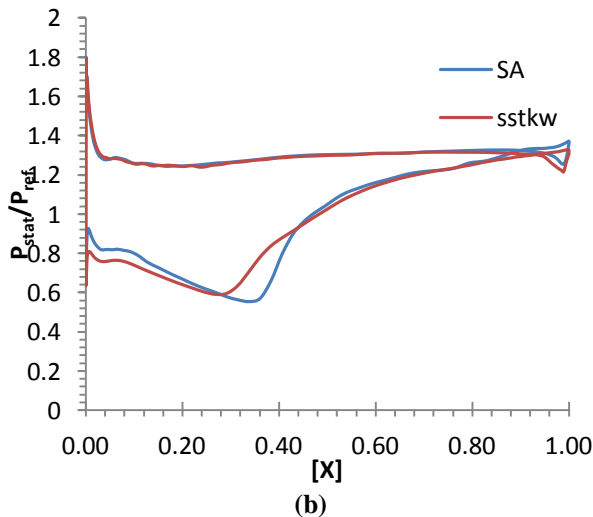


Fig. 12 70% spanwise at 7.5% & 110% chordwise position

Comparisons are also made between the turbulence models on the pressure distribution at each spanwise positions, see Fig. 13 a-c.

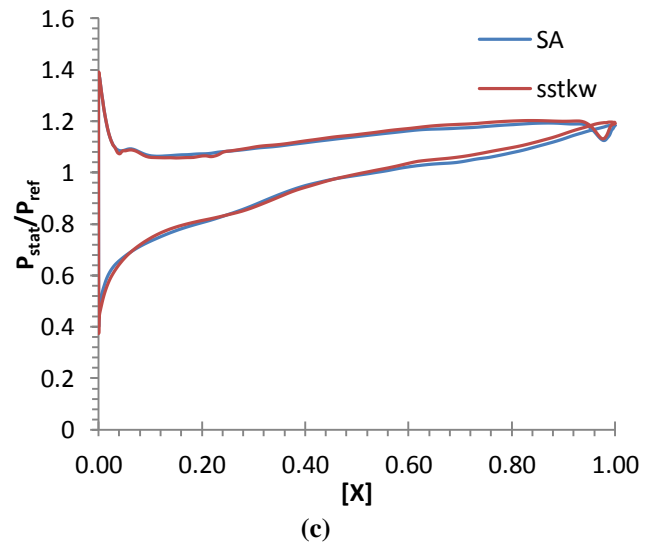


(a)



(b)

From Figure 8 (a) & (b), the differences between the turbulence models are quite visible. This shows the nature of each turbulence model in dealing with the level of flow complexity near the tip and mid-span regions of the blade, i.e. supersonic and transonic flow regions. In the next figure, the difference is insignificant as the flow is scaled down to subsonic. With approximately the same level of accuracy in the results, in terms of computational time, the SA simulation solves the case quicker than the k- ω SST simulation. This is mainly due to the number of transport equations within each model, i.e. SA is a one-equation model and k- ω SST is a two-equation model. People in the past have also preferred the one-equation model for the same case. Fidalgo [17] employed SA when looking at fan-distortion within the rotor. An FSI case of the rotor by Im [18] was also using SA when looking at the interaction between the blade vibrations with the travelling wave initial condition.



(c)

Fig. 13 Pressure distribution on the blade at 10% (a), 30% (b) and 70% (c) spanwise position.

2.4 Aerodynamic Forces

Having compared the current simulation with the experiment and the limited resources of measured aerodynamic forces, i.e. the pressure and viscous forces, acting on the blade, the following figures, Fig. 14 and Figure 15, show the profiles of the aerodynamic forces acting on the blade. These are obtained by employing a

UDF specifically purposed for the tapping of the aerodynamic forces.

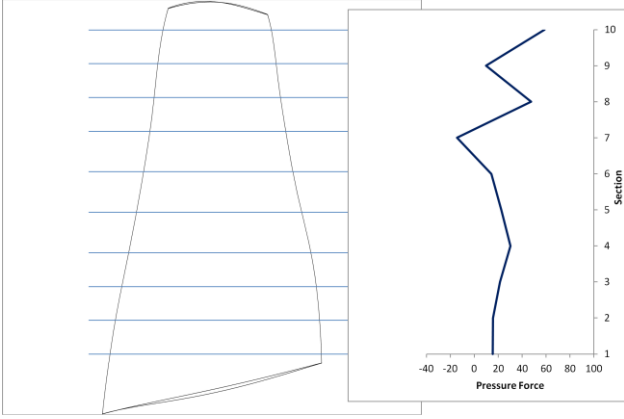


Fig. 14 Pressure force profile

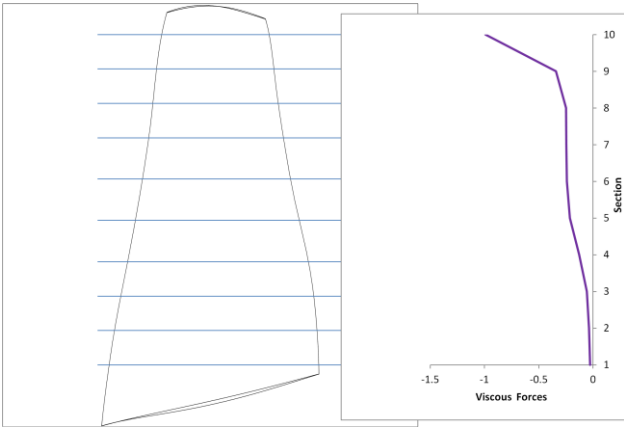


Fig. 15 Viscous force profile

3 1D Coupled Bending-Torsion

3.1 Coupled Equations without Rotation

One dimensional vibration is considered initially as the starting point prior to flutter analysis, in particular the compressor blade stall flutter. Dokumaci [19] took a case of standstill turbine blade to simulate the coupled vibration. The blade was attached at the hub and hanging free at its tip which can be assumed similar to a cantilever beam or wing of a plane. Assuming no aerodynamic forces, i.e. free vibration, were yet applied, the coupled bending-torsion vibration of the blade is written as follow,

$$\frac{\partial^2}{\partial y^2} \left(EI \frac{\partial^2 w}{\partial y^2} \right) + m \frac{\partial^2 w}{\partial t^2} + m x_\alpha \frac{\partial^2 \phi}{\partial t^2} = 0 \quad (2)$$

$$\frac{\partial}{\partial y} \left(GJ \frac{\partial \phi}{\partial y} \right) - m x_\alpha \frac{\partial^2 w}{\partial t^2} - I_\alpha \frac{\partial^2 \phi}{\partial t^2} = 0 \quad (3)$$

The equations can also be found in a book written by Fung [20].

w and ϕ are the bending and torsional displacements, EI and GJ are the bending and torsional rigidity of the beam, m and I_α are mass and mass moment of inertia of the beam, x_α is the distance between the elastic and inertia axis. The coupling terms in these equations are $m x_\alpha \frac{\partial^2 \theta}{\partial t^2}$ and $m x_\alpha \frac{\partial^2 w}{\partial t^2}$. In the paper, he presented a table consists of natural frequencies of the uncoupled and coupled equations. No substantial differences were seen from the uncoupled and coupled equations since x_α was small. However, the mode shapes of the coupled equations were showing considerable effect of the coupling in the bending and torsion displacements. Similar work was also carried out by Subrahmanyam et al. [21]. They found that coupling decreases the bending-dominated natural frequencies. Conversely, the torsion-dominated natural frequencies are increased by the coupling.

3.2 Coupled Equations with Rotation

Similar to the previous case of free vibration without rotation, a shape mode initialization is also required here. However, different equation of motion is used here since it involved the rotation of the beam. This can be found in reference [22], see Equations (4) and (5).

ρ is the radial coordinate in spanwise integration. Additional terms seen in Equation (4), namely $\frac{\partial}{\partial y} \left[\int_y^L m \Omega^2 \rho \partial \rho \frac{\partial w}{\partial y} \right]$ and $\frac{\partial}{\partial y} \left[\frac{d(y\theta)}{dy} \int_y^L \Omega^2 x_\alpha m \partial \rho \right]$, are centrifugal force and moment, respectively. $I_\alpha \theta \Omega^2$ and $y \frac{\partial}{\partial y} \left[\frac{dw}{dy} \int_y^L \Omega^2 x_\alpha m \partial \rho \right]$ from Equation (5) are nose-down propeller moment about the elastic axis and nose-up centrifugal moment, respectively.

3.3 Results

Natural frequencies of the coupled equations without rotation from selected reference is included. The parameters required within this equation are taken from Dokumaci

[19]. The same reference also provides exact natural frequency for a number of vibration shape mode.

$$\frac{\partial^2}{\partial y^2} \left(EI \frac{\partial^2 w}{\partial y^2} \right) - \frac{\partial}{\partial y} \left[\int_y^L m \Omega^2 \rho \partial \rho \frac{\partial w}{\partial y} \right] + m \frac{\partial^2 w}{\partial t^2} - m x_\alpha \frac{\partial^2 \theta}{\partial t^2} + \frac{\partial}{\partial y} \left[\frac{d(y\theta)}{dy} \int_y^L \Omega^2 x_\alpha m \partial \rho \right] = 0 \quad (4)$$

$$- \frac{\partial}{\partial y} \left(GJ \frac{\partial \theta}{\partial y} \right) + I_\alpha \frac{\partial^2 \theta}{\partial t^2} + I_\alpha \theta \Omega^2 - m x_\alpha \frac{\partial^2 w}{\partial t^2} + y \frac{\partial}{\partial y} \left[\frac{dw}{dy} \int_y^L \Omega^2 x_\alpha m \partial \rho \right] = 0 \quad (5)$$

Table 2 Natural frequency of coupled torsion at different time steps

NT	f (Hz)	Difference with Dokumaci [19] (%)
NT 2000	1615.39	4.94
NT 4000	1685.52	0.812
NT 6000	1685.52	0.812
NT 8000	1687.65	0.686

The smallest discrepancy with work presented by Dokumaci [19] is found on 8000 time steps. Following the increasing number of time steps, no further discrepancy is found significant from the current work. Hence, the optimum range number of time step is now bounded between.

To conclude the coupled bending-torsion solver analysis, the number spatial point is gradually increased while keeping the number of time step at 8000. The purpose is to see how much the result would differ from each spatial point given the optimum number of time step. It is evident from Table 2 and the respecting figure that the magnitude and the shape only differ slightly from the lowest to the highest number of spatial point. Further increase in the number of spatial points will not affect the

result to differ significantly. Hence, it can be said that the accuracy is unlikely to be strongly affected with the increasing spatial points while this also proves the problem dependency on the number of time step.

Table 3 Natural frequency of coupled bending at different spatial points

SP	f (Hz)	Difference with Dokumaci [19] (%)
SP 10	142.86	1.24
SP 50	144.13	0.357
SP 100	144.40	0.170
SP 150	144.40	0.170

Fig. 16 plots the coupled bending and torsion displacements on the same graph. The effect of the coupling is prominently shown by the waveform of the coupled torsion.

From Table 4, the differences of the solver with the previous numerical work by Rao and Banarjee [23] are quite reasonable.

Table 4 Natural frequency comparison

Ω	Mode	f (Hz)	Difference with Rao and Banarjee [23] (%)
262 rad/s	1 st mode bending	157.74	0.17
	1 st mode torsion	1687.65	0.67
366 rad/s	1 st mode bending	168.65	0.80
	1 st mode torsion	1687.65	0.67

The largest percentage of difference shown there is on the 1st mode bending with the rotational velocity of 366 rad/s. Interestingly, the natural frequency of the coupled torsion shows no evidence that it has been affected by the rotational velocity, unlike the coupled bending. As the rotational velocity increases, so does the coupled bending natural frequency. This is also clearly depicted from Fig. 17. It implies that the rotational velocity may have not

yet coincide with the natural frequency of the rotating beam. A Campbell diagram has this purpose of showing the rotational velocity against the natural frequency of each mode vibration. Hence, further measure can be conducted to prevent the vibration severely cause the beam to failure.

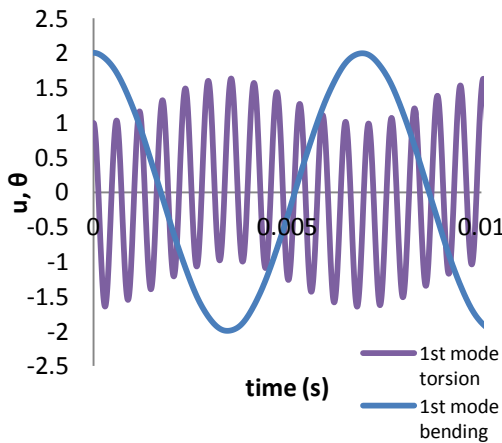


Fig. 16 Displacements of coupled bending-torsion at $x/L=1$

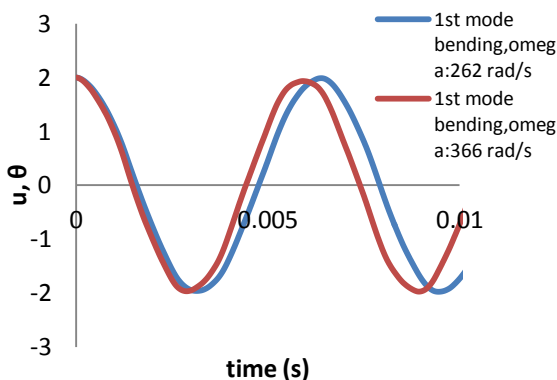


Fig. 17 Comparison of 1st bending mode for different rotational velocity

4 Conclusion and Future Works

The current work reveals that the present work has suffered from numerical set up flaws given the qualitative discrepancy observed with the selected experimental work. Nevertheless, the numerical work do manage to capture some of the flow physics, such as the supersonic bubble which occurs on the 70% spanwise from the hub. It is also observed that inlet velocity on the 10% and 30% is pretty much similar to experimental work. However, discrepancy is

still observed from the current simulation, in particular the outlet flow profiles. These are mainly due to the inadequate distance from the blade trailing edge to outlet boundary. Other discrepancy is in accordance to tip clearance availability. Nevertheless, from the flow profiles within the blade passage, the simulations are qualitatively matched. There are some differences, but this is still tolerable. Between two turbulence models, it is more likely the following work is going to use the one-equation Spalart Allmaras (SA). The aerodynamic forces profiles have also being depicted here, as this will be the input for the coupled equations in obtaining the natural frequency of each vibration modes.

The coupled bending-torsion equations are essentially 4th order parabolic and 2nd order hyperbolic partial differential equations (PDE). These equations are discretized with finite difference method by which is the simplest discretization method. Only the one dimensional equations are considered here initially. In the first year work, the equations were decoupled and the results were quite satisfying given the small discrepancies with the analytical and selected references. Following the success here is the coupling of these codes, the bending and torsional solvers, and the introduction of several source terms as well as the rotational effect. The results presented here are reasonably satisfying. The coupling effect is well-captured by the code as well as the rotational effect. It is observed, as the rotational velocity increases, so does the coupled bending natural frequency. This is unlikely to happen in the coupled torsion natural frequency. It implies here that the rotational velocity set at these cases is not coinciding with the coupled torsion natural frequency. A diagram known as the Campbell diagram has the role in depicting the overlay of the rotational velocity and each mode natural frequency.

5 Acknowledgement

The author would like to acknowledge the Ministry of Education Republic of Indonesia and the Education Attache of Indonesian Embassy in London for the financial support in carrying out the research.

6 References

- [1] M. Chen, "Development of fan/compressor techniques and suggestions on further researches," *Journal of Aerospace Power*, pp. 1-15, 2002.
- [2] H. Doi, "Fluid/structure coupled aeroelastic computations for transonic flows in turbomachinery," 2002.
- [3] J. G. Marshall and M. Imregun, "A review of aeroelasticity methods with emphasis on turbomachinery applications," *Journal of fluids and structures*, vol. 10, pp. 237-267, 1996.
- [4] E. H. Dowel, H. C. Curtiss, R. H. Scanlan and F. Sisto, *A modern course in aeroelasticity*, Kluwer academic publishers, 1989, pp. 411-442.
- [5] M. P. Boyce, "Axial-Flow Compressors," in *Gas Turbine Engineering Handbook*, Gulf Professional Publishing, 2006, pp. 274-335.
- [6] A. Khalak, "A Framework for Flutter Clearance of Aeroengine Blades," *Journal of Engineering for Gas Turbines and Power*, vol. 124, pp. 1003-1010, 2002.
- [7] H. E. Martensson, J. Ostlund, R. Bladh and B. Gruber, "Design and Analysis of a Transonic Flutter Research Compressor," MTU Aero Engines.
- [8] A. J. Strazisar, J. R. Wood, M. D. Hathaway and K. L. Suder, "Laser anemometer measurements in a transonic axial-flow fan rotor," NASA, 1989.
- [9] M. J. Pierzga and J. R. Wood, "Investigation of the three dimensional flow field within a transonic fan rotor: experimental and analysis," NASA, Cleveland, 1985.
- [10] K. Yamada, M. Furukawa, M. Inoue and K.-i. Funazaki, "Numerical analysis of tip leakage flow field in a transonic axial compressor rotor," in *International Gas Turbine Congress*, Tokyo, 2003.
- [11] H. Khaleghi, M. Boroomand, A. M. Tousi and J. A. Teixeira, "Stall inception in a transonic axial fan," *Proceeding of the Institution of Mechanical Engineers, Part A: Journal of Power and Energy*, vol. 222, pp. 199-208, 2008.
- [12] J. Du, F. Lin, H. Zhang and J. Chen, "Numerical simulation on the effect of tip clearance size on unsteadiness in tip clearance flow," *Journal of Thermal Science*, vol. 17, no. 4, pp. 337-342, 2008.
- [13] R. V. Chima, "Viscous three-dimensional calculations of transonic fan performance," in *77th Symposium of the Propulsion and Energetics Panel entitled CFD Techniques for Propulsion Applications*, San Antonio, 1991.
- [14] A. J. F. Reis, "Validation of NASA rotor 67 with OpenFOAM's transonic density-based solver," 2013.
- [15] G. Tang, "Measurements of the tip-gap turbulent flow structure in a low-speed compressor cascade," 2004.
- [16] J. J. Adamczyk, M. L. Celestina and E. M. Greitzer, "The role of tip clearance in high-speed fan stall," in *ASME 91-GT-83*, 1991.
- [17] V. J. Fidalgo, C. A. Hall and Y. Colin, "A Study of Fan-Distortion Interaction within the NASA Rotor 67 Transonic Stage," *Journal of Turbomachinery*, vol. 134, p. 12, 2012.
- [18] H.-S. Im and G.-C. Zha, "Prediction of a Transonic Rotor Fluid/Structure Interaction with a Traveling Wave using a Phase-lag Boundary Condition," in *51st AIAA Aerospace Sciences Meeting including the New Horizons Forum and Aerospace Exposition*, Texas, 2013.
- [19] E. Dokumaci, "An exact solution for coupled bending and torsion vibrations of uniform beams having single cross-sectional symmetry," *Journal of Sound and Vibration*, pp. 443-449, 1987.
- [20] Y. Fung, *An introduction to the theory of aeroelasticity*, New York: John Wiley & Sons, Inc, 1955.
- [21] K. B. Subrahmanyam, S. V. Kulkarni and J. S. Rao, "Coupled bending-torsion vibrations of rotating blades of asymmetric aerofoil cross section with allowance for shear deflection and rotary inertia by use of the Reissner method," *Journal of Sound and Vibration*, vol. 75, no. 1, pp. 17-36, 1981.
- [22] W. Johnson, *Helicopter Theory*, Dover Publications, 2004.
- [23] J. S. Rao and S. Banarjee, "Coupled bending-torsional vibrations of rotating cantilever blades-method of polynomial frequency equation," *Mechanism and Machine Theory*, vol. 12, pp. 271-280, 1977.

7 Contact Author Email Address

All emails corresponding to paper can be addressed to:

radya.wiranegara@manchester.ac.uk

Copyright Statement

The authors confirm that they, and/or their company or organization, hold copyright on all of the original material included in this paper. The authors also confirm that they have obtained permission, from the copyright holder of any third party material included in this paper, to publish it as part of their paper. The authors confirm that they give permission, or have obtained permission from the copyright holder of this paper, for the publication and distribution of this paper as part of the ICAS 2014 proceedings or as individual off-prints from the proceedings.